



Volume and rate of volcanic CO₂ emissions governed the severity of past environmental crises

Qiang Jiang^{a,b,c,1,2}, Fred Jourdan^{a,b,c}, Hugo K. H. Olierook^{b,c,d}, Renaud E. Merle^e, Julien Bourdet^f, Denis Fougereuse^{b,c,g}, Belinda Godel^h, and Alex T. Walker^c

Edited by Paul Renne, University of California, Berkeley, CA; received February 4, 2022; accepted June 13, 2022 by Editorial Board Member Michael Manga

The emplacement of large igneous provinces (LIPs) has been linked to catastrophic mass extinctions in Earth's history, but some LIPs are only associated with less severe oceanic anoxic events, and others have negligible environmental effects. Although it is widely accepted that massive magma outpouring can affect the environment through volatile degassing, it remains debated what controls the severity of environmental crises. Here, we demonstrate that the second-most-voluminous Phanerozoic LIP, the Kerguelen LIP, may have contributed to the early Aptian oceanic anoxic event 1a, a global event previously believed to have been caused by the Ontong Java LIP. Geochronological data show that the earliest eruptions of the Kerguelen LIP preceded the onset of oceanic anoxic event 1a by at least ~5 million years. Analyses of CO₂ abundances in melt inclusions combined with Monte Carlo simulations reveal that the volume and degassing rate of CO₂ emissions from the Kerguelen LIP are an order of magnitude lower compared to LIPs that caused severe mass extinctions. We propose that the severity of volcanism-related environmental and biotic perturbations is positively correlated with the volume and rate of CO₂ emissions. Our results highlight the significant importance of reducing and slowing down CO₂ emission in preventing future disastrous environmental consequences.

large igneous province | CO₂ emission | ⁴⁰Ar/³⁹Ar geochronology | Kerguelen Plateau | oceanic anoxic event

Large igneous provinces (LIPs) are gigantic magmatic events that have often been linked to drastic and sudden environmental and biotic perturbations (1, 2). High-precision geochronology data have revealed concurrences between LIPs and catastrophic mass extinctions [e.g., Central Atlantic magmatic province (CAMP) and the end-Triassic mass extinction (3)] and between LIPs and less severe oceanic anoxic events [OAEs; e.g., Karoo–Ferrar LIPs and the Toarcian OAE (4, 5)]. However, there are also some LIPs that are seemingly not associated with any biotic or environmental perturbations [e.g., Parana–Etendeka (6) and Tarim LIP (7); Fig. 1A]. It is still unclear why the emplacement of LIPs resulted in such diverse environmental responses (8). Possible explanations may include differences in pre-eruption atmospheric CO₂ levels (9); the volume, tempo, rate, and composition of volcanic volatiles released by LIPs (10–15); and factors affecting volcanogenic carbon sinks (9, 16, 17). Many of the interpretations on the causal links between LIPs and the severity of environmental and biotic crises were based on coupled volatile–geochronological studies of LIPs associated with disastrous environmental perturbations [e.g., CAMP, Siberian Traps, or Emeishan (18–20)], but this combined approach has not yet been applied to LIPs for which environmental consequences are not obvious or are less extreme, such as OAEs.

The early Aptian OAE 1a, together with the Toarcian and Cenomanian–Turonian OAEs (21), is one of three confirmed OAEs that are global in scale, all of which are characterized by worldwide deposition of organic-rich black shales and large carbon-isotope anomalies in marine and terrestrial organic matter and carbonate (22, 23). The OAEs represent periods of large expanses of the world's oceans that were depleted of dissolved oxygen and may have been associated with the extinctions of marine organisms (24). The start of OAE 1a has recently been constrained to 120.4 ± 0.4 million years ago (Ma) (calculated from refs. 25 and 26; *Materials and Methods*; uncertainty for ages herein are quoted at 2σ). The supposed synchronicity and volcanic signatures in sedimentary rocks have led many to believe that OAE 1a was caused by CO₂ degassing from the Ontong Java LIP (27–31), which is believed to have initiated at ~127.2 ± 2.2 Ma (recalculated from ref. 32; cf. ref. 33). However, the age constraints for the Ontong Java LIP were based on ⁴⁰Ar/³⁹Ar dating of groundmass, instead of mineral separates, the former being problematic due to the presence of cryptic hydrothermal

Significance

Massive volcanic eruptions termed large igneous provinces have been variously linked to catastrophic mass extinctions, linked to less severe oceanic anoxic events, or not associated with any environmental perturbation. It remains unclear what controls the severity of environmental perturbations caused by these magmatic events. This paper shows that the Kerguelen large igneous province was coeval with and may have contributed to the early Cretaceous oceanic anoxic event 1a. However, due to a lower volume and rate of CO₂ emissions compared with those of extinction-causing large igneous provinces, the environmental perturbation of the Kerguelen large igneous province is much less significant. This demonstrates the critical importance of reducing and slowing down CO₂ emissions in preventing disastrous environmental crises.

Author contributions: Q.J., F.J., H.K.H.O., and R.E.M. designed research; Q.J., F.J., and H.K.H.O. performed research; Q.J., F.J., H.K.H.O., J.B., D.F., B.G., and A.T.W. contributed new reagents/analytic tools; Q.J., F.J., H.K.H.O., R.E.M., J.B., D.F., and B.G. analyzed data; Q.J. wrote the paper; and F.J., H.K.H.O., R.E.M., J.B., D.F., B.G., and A.T.W. reviewed and edited the paper.

The authors declare no competing interest.

This article is a PNAS Direct Submission. P.R. is a guest editor invited by the Editorial Board.

Copyright © 2022 the Author(s). Published by PNAS. This article is distributed under Creative Commons Attribution-NonCommercial-NoDerivatives License 4.0 (CC BY-NC-ND).

²Present address: College of Geosciences, China University of Petroleum, Beijing 102249, China

¹To whom correspondence may be addressed. Email: q.jiang@cup.edu.cn.

This article contains supporting information online at <http://www.pnas.org/lookup/suppl/doi:10.1073/pnas.2202039119/-/DCSupplemental>.

Published July 25, 2022.

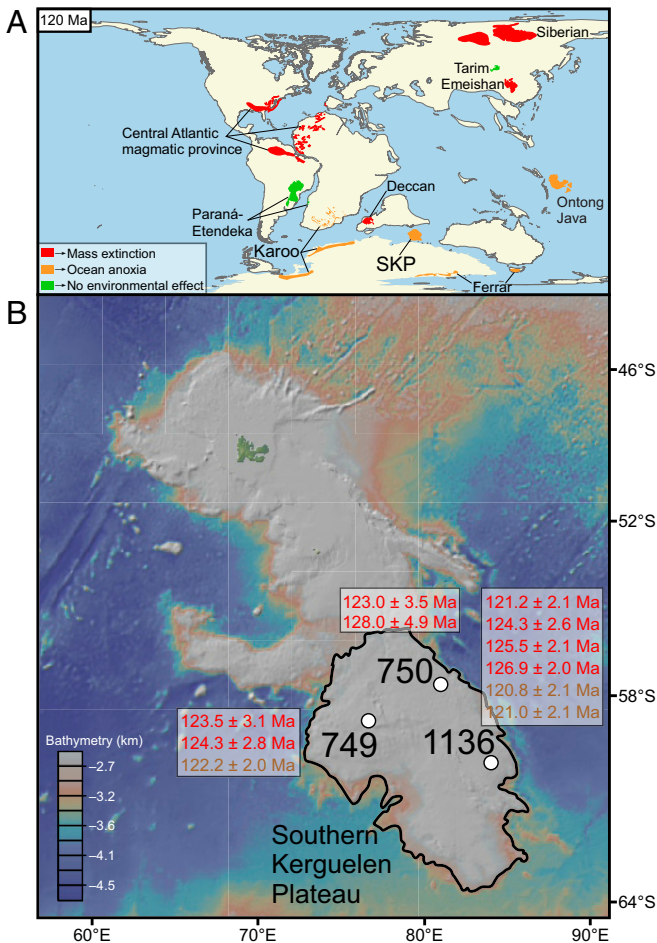


Fig. 1. Paleogeographic position and bathymetric map of the Southern Kerguelen Plateau (SKP). (A) Global plate reconstruction at 120 Ma, based on the model of ref. 91, and distribution of major LIPs. Note that the Deccan Traps did not appear until ~66 Ma. (B) Bathymetric map of the Southern Kerguelen Plateau, annotated with $^{40}\text{Ar}/^{39}\text{Ar}$ ages in this study (in red) and from refs. 40 and 42 (in brown).

alteration, which would make the ages erroneously young (e.g., refs. 34–36). The lack of high-precision and reliable isotopic ages for the Ontong Java LIP prevents establishing a causal relationship to OAE 1a. The High Arctic LIP has also been proposed as a trigger for OAE 1a (37). However, recent mercury studies indicate an absence of intense magmatism for the High Arctic LIP at the time of OAE 1a (38).

The second-most-voluminous LIP of the Phanerozoic, the Kerguelen LIP, with a total volume of $\sim 17.4 \times 10^6 \text{ km}^3$ (39), has not been regarded as a trigger for OAE 1a, but is believed to only be the cause of subtle environmental perturbation in the late Aptian immediately after OAE 1a (27). These interpretations were based on an $^{40}\text{Ar}/^{39}\text{Ar}$ plateau age of $119.0 \pm 2.1 \text{ Ma}$ (40) from the Southern Kerguelen Plateau (Fig. 1B), which was the oldest isotopic age available for the Kerguelen LIP at the time. Refined ^{40}K decay constants (41) shifts this age to $121.0 \pm 2.1 \text{ Ma}$ (SI Appendix). Recently, a different site from the Southern Kerguelen Plateau yielded an $^{40}\text{Ar}/^{39}\text{Ar}$ plateau age of $122.2 \pm 2.0 \text{ Ma}$ (Fig. 1B and ref. 42). Although both of these ages are not precise enough to resolve the temporal relationship between the Kerguelen LIP and OAE 1a, they raise the possibility that our current understanding about the chronology of the Southern Kerguelen Plateau may not be accurate and that the Kerguelen LIP may be linked to OAE 1a.

Results

The $^{40}\text{Ar}/^{39}\text{Ar}$ Ages of the Southern Kerguelen Plateau. We obtained eight $^{40}\text{Ar}/^{39}\text{Ar}$ plateau ages of plagioclase separates from basalts (*Materials and Methods* and *SI Appendix*, Fig. S1 and Table S1) from Ocean Drilling Project Sites 749, 750, and 1136 on the Southern Kerguelen Plateau (Fig. 1B), where robust geochronology data are scarce (*SI Appendix*, Figs. S1–S5 and Tables S2 and S3).

Site 749 yielded two $^{40}\text{Ar}/^{39}\text{Ar}$ plateau ages of $123.5 \pm 3.1 \text{ Ma}$ and $124.3 \pm 2.8 \text{ Ma}$ (Fig. 2 and *SI Appendix*, Fig. S2 and Table S2). They overlap with each other and with the age of $122.2 \pm 2.0 \text{ Ma}$ reported by ref. 42 at 2σ (*SI Appendix*, Fig. S3). The age of $124.3 \pm 2.8 \text{ Ma}$ (749C-16R-7, 37–47) is older than the age of OAE 1a at $120.4 \pm 0.4 \text{ Ma}$ (*SI Appendix*, Fig. S4), suggesting that volcanism at Site 749 initiated before OAE 1a.

Samples from Site 750 yielded a miniplateau age of $123.0 \pm 3.5 \text{ Ma}$ and a plateau age of $128.0 \pm 4.9 \text{ Ma}$ (Fig. 2 and *SI Appendix*, Fig. S2 and Table S2), the latter indicating active volcanism at Site 750 prior to OAE 1a (*SI Appendix*, Fig. S4).

For Site 1136, we obtained four plateau ages of $121.2 \pm 2.1 \text{ Ma}$, $125.5 \pm 2.1 \text{ Ma}$, $124.3 \pm 2.6 \text{ Ma}$, and $126.9 \pm 2.0 \text{ Ma}$ (Fig. 2 and *SI Appendix*, Fig. S2 and Table S2). These ages suggest that the Southern Kerguelen Plateau volcanism began erupting no later than $\sim 124.9 \text{ Ma}$ (i.e., the lower limit of $126.9 \pm 2.0 \text{ Ma}$ yielded by sample 1136A-19R-1, 139–149; *SI Appendix*, Fig. S4), ~ 5 million years prior to OAE 1a.

CO_2 Emission of the Southern Kerguelen Plateau. We studied the volcanic degassing of the Kerguelen LIP based on volatiles encapsulated in plagioclase-hosted melt inclusions (Fig. 3).

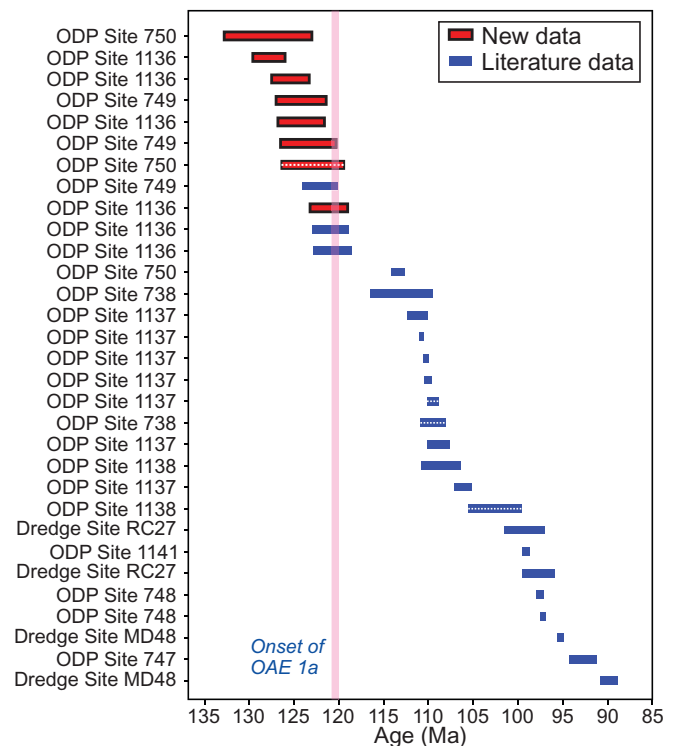


Fig. 2. The $^{40}\text{Ar}/^{39}\text{Ar}$ ages for the Kerguelen LIP and age of OAE 1a. The literature ages of the Kerguelen LIP are from refs. 39, 40, and 42. The $^{40}\text{Ar}/^{39}\text{Ar}$ ages have been filtered for robustness (*SI Appendix*). The onset age of OAE 1a is calculated from refs. 25 and 26 (*Materials and Methods*). Boxes with dashed white lines indicate $^{40}\text{Ar}/^{39}\text{Ar}$ miniplateau ages (with 50 to 70% ^{39}Ar released). Width of boxes indicates 2σ uncertainties. ODP, Ocean Drilling Project.

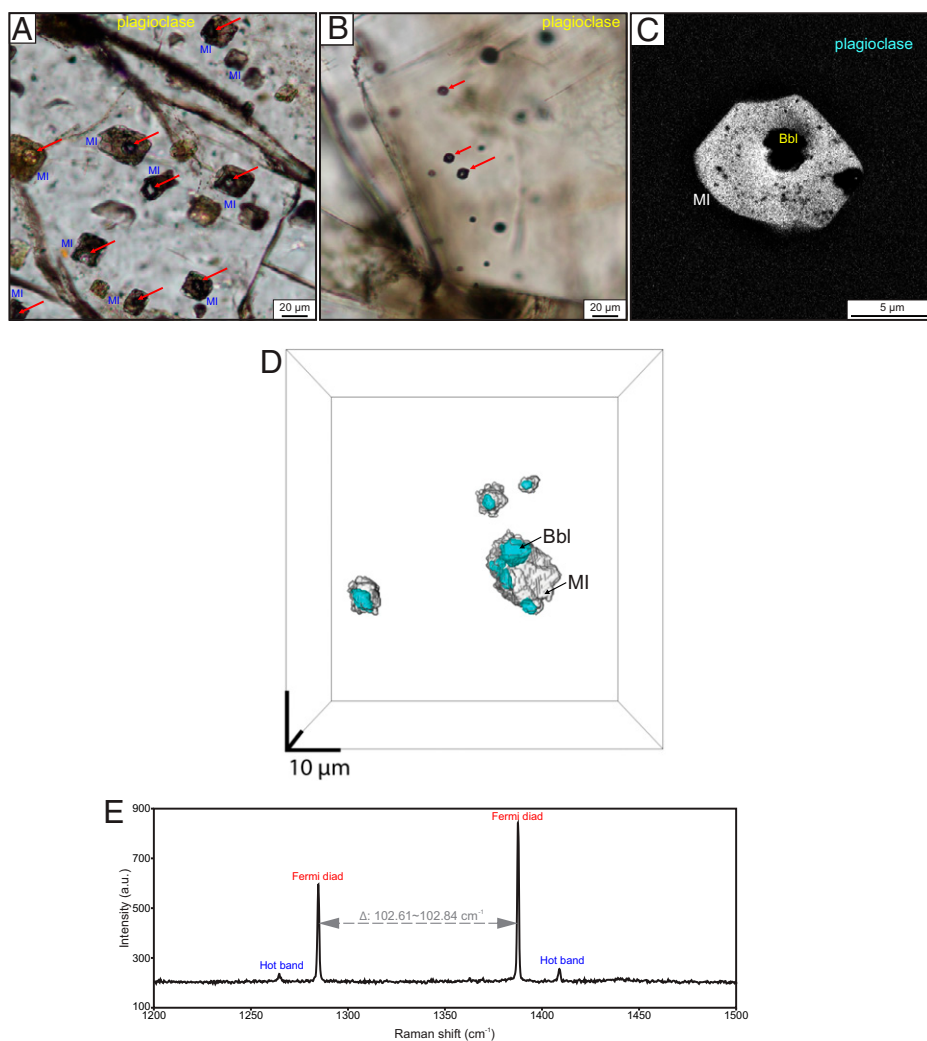


Fig. 3. Representative images of plagioclase-hosted melt inclusions and gas inclusions and micro-Raman spectrum of a CO₂-bearing bubble in a melt inclusion. (A) Plane-polarized light images of bubbles (red arrows) in plagioclase-hosted melt inclusions (MI). (B) Plane-polarized light images of gas inclusions (red arrows) in plagioclase. (C) Backscattered-electron images showing exposed bubbles (Bbls) in plagioclase-hosted melt inclusions. (D) HRXCT 3D image of bubble-bearing melt inclusions. (E) Micro-Raman spectrum of a CO₂-bearing bubble in a melt inclusion. The presence of CO₂ is indicated by the Fermi diad and hot bands. A.u., arbitrary units.

Melt inclusions that were originally in equilibrium with the host magma are a record of pre-eruptive volatile concentrations. We used Raman spectroscopy to study the compositions of the bubbles in the melt inclusions (*Materials and Methods*) and detected only CO₂, while other volcanic gases, such as CO, CH₄, and H₂S, were not detected (*SI Appendix, Fig. S6*). The densities of CO₂ in the bubbles were calculated by using Fermi diad splitting (Fig. 3E) and a calibrated CO₂ densimeter (*SI Appendix, Fig. S7*), which ranged from 0.01 to 0.09 g·cm⁻³ (*SI Appendix, Table S4*). The volume percent (vol.%) of the bubble(s) in a melt inclusion was determined through High-Resolution X-Ray Computed Tomography (HRXCT) (Fig. 3D, *SI Appendix, Fig. S8*, and *Materials and Methods*). The abundance of CO₂ in the melt inclusions, which is representative of the Kerguelen magma, was calculated through Monte Carlo simulations using the parameters and their distributions in *SI Appendix, Table S5* (*Materials and Methods*) and resulted in 0.15^{+0.17}_{-0.08} wt.% (uncertainty for CO₂ abundances, volumes, and rates herein is quoted at 1σ).

A Monte Carlo simulation approach was also used to calculate the total amount of CO₂ in the pre-120-Ma portion of the Southern Kerguelen Plateau magma (*SI Appendix, Fig. S5* and *Table S5*), which resulted in a total amount of 0.29^{+0.34}_{-0.16} × 10⁵ Gt CO₂

(*Table 1* and *Materials and Methods*). Assuming a CO₂ degassing efficiency of 80 to 100% (refs. 12 and 43 and *Materials and Methods*), a total amount of 0.26^{+0.31}_{-0.14} × 10⁵ Gt CO₂ (*Table 1* and *SI Appendix, Fig. S9*) was degassed from the Southern Kerguelen Plateau.

Monte Carlo Simulation of CO₂ Emissions of Extinction-Causing LIPs.

Published estimations of CO₂ emissions of LIPs that are associated with mass extinctions are commonly reported at the maximum and/or minimum values without associated uncertainties (e.g., refs. 18–20). To allow for a direct comparison with our estimation of CO₂ emission of the Southern Kerguelen Plateau, we used a Monte Carlo simulation method and literature measurements/modelings to calculate the CO₂ emissions and associated uncertainties of these LIPs (*Materials and Methods* and *SI Appendix, Tables S6–S9*). Our results show that the volume of CO₂ emitted from the Southern Kerguelen Plateau (0.26^{+0.31}_{-0.14} × 10⁵ Gt) is an order of magnitude smaller than the amounts of CO₂ derived from magmatic source and contact metamorphism of sediments associated with the Siberian Traps (2.08^{+0.40}_{-0.34} × 10⁵ Gt; recalculated from refs. 19 and 44), CAMP (1.64^{+0.42}_{-0.38} × 10⁵ Gt or 1.05^{+0.35}_{-0.34} × 10⁵ Gt; recalculated from refs. 18 and 45, with the

Table 1. Summary of CO₂ emission volumes and rates of major LIPs computed using Monte Carlo simulations

	Total CO ₂ emission (× 10 ⁵ Gt)	Average CO ₂ emission rate (Gt·y ⁻¹)	Amount of CO ₂ in magma (× 10 ⁵ Gt)	Magmatic CO ₂ degassed (× 10 ⁵ Gt)	Sedimentary rock-derived CO ₂ (× 10 ⁵ Gt)
Southern Kerguelen Plateau	0.26 ^{+0.31} _{-0.14}	0.004 ^{+0.005} _{-0.002}	0.29 ^{+0.34} _{-0.16}	0.26 ^{+0.31} _{-0.14}	—
Siberian Traps	2.08 ^{+0.40} _{-0.34}	0.23 ^{+0.05} _{-0.04}	1.34 ^{+0.33} _{-0.26}	1.30 ^{+0.35} _{-0.28}	0.77 ^{+0.23} _{-0.22}
Emeishan LIP	1.30 to 1.88	0.13 ^{+0.12} _{-0.05}	0.56 to 0.74	0.55 ^{+0.10} _{-0.09}	0.75 to 1.33
Deccan Traps	0.13 to 0.35	0.01 to 0.04	0.15 to 0.40	0.13 to 0.35	—
CAMP	1.64 ^{+0.42*} _{-0.38}	0.25 ^{+0.07*} _{-0.06}	0.97 ^{+0.37*} _{-0.29}	0.87 ^{+0.34*} _{-0.26}	0.75 ^{+0.26} _{-0.25}
	1.05 ^{+0.35†} _{-0.34}	0.16 ^{+0.05†} _{-0.05}	0.31 ^{+0.27†} _{-0.23}	0.28 ^{+0.25†} _{-0.21}	

Uncertainties are quoted at 1 σ . Some values for the Emeishan LIP and Deccan Traps are reported at the 16 to 84 percentiles due to their flat-topped distributions.

*Calculated using the Raman CO₂ densimeter of ref. 65.

†Calculated using the CO₂ densimeter of this study.

differences in estimates based on different Raman CO₂ densimeters), and the Emeishan LIP ([1.30 to 1.88] × 10⁵ Gt [16 to 84 percentiles]; recalculated from refs. 20 and 46) and is the same order of magnitude with that of the Deccan Traps ([0.13 to 0.35]) × 10⁵ Gt [16 to 84 percentiles]; recalculated from ref. 47; Table 1 and *SI Appendix, Fig. S9*).

Discussion

Our geochronology data show that, for all three sites on the Southern Kerguelen Plateau, there are one or more lava flows that are distinctly older than OAE 1a (Fig. 2 and *SI Appendix, Fig. S4*). The ages reveal that the Southern Kerguelen Plateau volcanism may have started erupting from as early as ~128 Ma and had been relatively continuous before, during, and even after OAE 1a (ref. 42; Fig. 2), and there seems to be an increase of activity around that time (*SI Appendix, Fig. S4B*). Thus, there is temporal correlation between the Kerguelen LIP and OAE 1a. A series of geochemical changes in lower Aptian sediments, such as negative excursions in osmium (28) and strontium isotopes (48, 49) and mercury (29) and trace metal enrichments (27), all indicate that the occurrence of OAE 1a was caused by increased magmatic activity. It is likely that the Kerguelen LIP could have contributed to the occurrence of OAE 1a due to their temporal correlation.

The carbon-isotope record of OAE 1a is characterized by an abrupt negative excursion of up to -3‰ in marine carbonates and of -4 to -5‰ in the organic carbon, prior to a large positive excursion (31). The negative $\delta^{13}\text{C}$ excursion was believed to be caused by the input of volcanogenic CO₂ that is isotopically light into the ocean-atmosphere system (27). The melt-inclusion studies reveal that a total amount of 0.26^{+0.31}_{-0.14} × 10⁵ Gt CO₂ was emitted from the Southern Kerguelen Plateau volcanism before OAE 1a. Our calculations show that these CO₂ emissions could only have led to a decrease of the $\delta^{13}\text{C}$ value from ~2.5‰ (22) to ~1.36‰ for the early Cretaceous CO₂ reservoir (*Materials and Methods*), but were not able to cause a negative excursion of -3 to -5‰ that was observed for OAE 1a. Therefore, the CO₂ emission of Southern Kerguelen Plateau magmatism alone was insufficiently voluminous to be the trigger of OAE 1a.

If the theory that OAE 1a was caused by coeval magmatism is correct, then a possible scenario is that the magmatic trigger is the Southern Kerguelen Plateau together with the previously believed trigger—the Ontong Java LIP (e.g., refs. 27 and 28). Given that the Southern Kerguelen Plateau eruptions were mostly subaerial, where volcanic gases were directly emitted

into the atmosphere, while the bulk of the Ontong Java LIP was emplaced in a submarine environment, as revealed by drill holes (e.g., refs. 40 and 50), it is likely that the Ontong Java LIP may have played a larger role in marine anoxia by directly degassing into the ocean, whereas the Kerguelen LIP contributed more to coeval terrestrial environmental perturbations with OAE 1a, as indicated by data from terrestrial records (e.g., ref. 23). This hypothesis and the possible role dichotomy between the two provinces can only be investigated with both accurate age and CO₂ emission estimations from the Ontong Java LIP.

We demonstrated above that, despite the significant magmatic volume of the Southern Kerguelen Plateau, it did not cause any extinction event and may even lack the ability to cause an OAE. This is in contrast with other LIPs that also have gigantic magma volumes, but caused disastrous environmental consequences, such as the Siberian Traps, the Emeishan LIP, CAMP, and the Deccan Traps. The difference in the environmental response of these magmatic events could be related to their difference in the amount of CO₂ emissions (Fig. 4). The Southern Kerguelen Plateau volcanism caused an input of ~0.26 × 10⁵ Gt CO₂ to the atmosphere, which is an order of magnitude lower than that of extinction-causing LIPs, such as the Emeishan LIP ([1.30 to 1.88] × 10⁵ Gt), the Siberian Traps (~1.99 × 10⁵ Gt), and CAMP (~1.64 × 10⁵ Gt or ~1.05 × 10⁵ Gt). Indeed, the Siberian Traps, which have the highest CO₂ emission volume, are associated with Earth's deadliest extinction event at the Permian-Triassic boundary that witnessed the loss of up to 96% of marine invertebrate species (e.g., ref. 51; Fig. 4). The Deccan Traps, on the other hand, have a relatively low volume of CO₂ emission (Fig. 4) that is similar to that of the Southern Kerguelen Plateau, despite its possible link with the end-Cretaceous mass extinction. This suggests that the Deccan Traps probably also played a moderate role in the end-Cretaceous mass extinction and that the Chicxulub impact event was indeed the main trigger for such a severe global environmental and biotic disaster (e.g., refs. 35 and 52).

The other factor that might have affected the severity of environmental consequences of LIPs is the rate of CO₂ degassing caused by the emplacement of LIPs. It remains challenging to calculate the rate of CO₂ emission of LIPs, mainly because of the existence of magmatic quiescent periods that may last hundreds to thousands of years (e.g., ref. 11) and are not resolvable by current geochronological methods. Here, we calculate the average CO₂ emission rate using the estimated CO₂

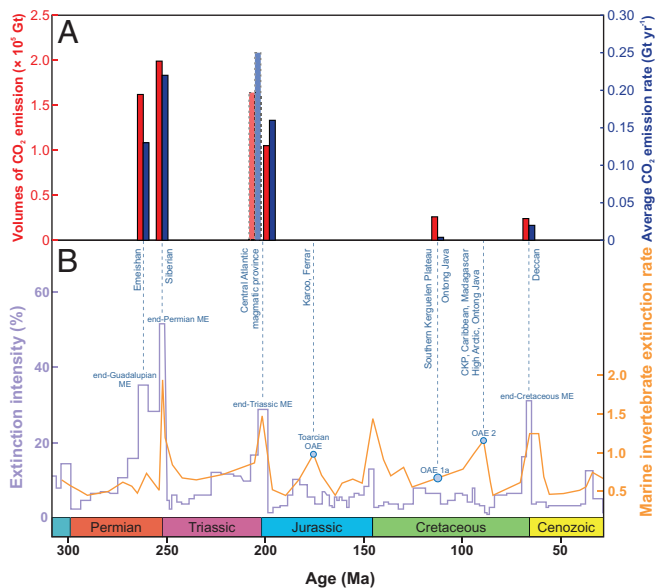


Fig. 4. Ages and CO₂ emissions of LIPs and associated mass extinctions (MEs) and OAEs. (A) The volumes (red) and average rates (blue) of CO₂ emissions of LIPs. The columns for CAMP indicate the volumes and rates of CO₂ emissions calculated using the CO₂ densimeter of this study, while the values calculated using the CO₂ densimeter of ref. 65 are represented using semitransparent bars with dashed outlines. The CO₂ estimations corresponding to OAE 1a are only from the Southern Kerguelen Plateau due to the lack of data for the Ontong Java LIP. References for the ages of LIPs and the calculations of CO₂ emission volumes and rates are detailed in *Materials and Methods*. (B) The mass extinction intensity refers to the fraction of genera that were present in each period of time, but were absent in the following time interval (92). The marine invertebrate extinction rates are from ref. 13.

emission volumes and the durations of LIPs to characterize the overall CO₂ degassing intensity over the course of LIP emplacements (*Materials and Methods*). The results reveal that the Southern Kerguelen Plateau volcanism has the lowest average CO₂ degassing rate ($0.004^{+0.005}_{-0.002}$ Gt·y⁻¹) prior to OAE 1a, while extinction-causing LIPs, such as the Emeishan LIP ($0.13^{+0.12}_{-0.05}$ Gt·y⁻¹), the Siberian Traps ($0.23^{+0.05}_{-0.04}$ Gt·y⁻¹), and CAMP ($0.25^{+0.07}_{-0.06}$ Gt·y⁻¹ or $0.16^{+0.05}_{-0.05}$ Gt·y⁻¹, using different Raman CO₂ densimeters) all have average CO₂ emission rates that are 1 to 2 orders of magnitude higher (Fig. 4 and Table 1). The Deccan Traps again is an exception in having a relatively low CO₂ degassing rate (0.01 to 0.04 Gt·y⁻¹ [16 to 84 percentiles]; Fig. 4), probably indicating a more central role to the Chicxulub impact in causing the end-Cretaceous mass extinction.

The relatively low volume and low rate of CO₂ degassing from the Southern Kerguelen Plateau volcanism meant that atmospheric CO₂ levels would not rapidly increase to levels sufficient to immediately trigger severe environmental consequences. Over the course of the Southern Kerguelen Plateau emplacement, several negative feedbacks could have mitigated a dramatic increase in atmospheric CO₂. First, a mild increase in atmospheric CO₂ and temperature and increased nutrient (e.g., Fe, Zn, and P) input, due to ash dispersal from subaerial eruptions and basalt weathering, created beneficial conditions for biological growth that, in turn, would lead to increased carbon burial and expanded anoxia in shallow waters (13, 21). Second, silicate and basalt weathering can act as an important mechanism of CO₂ consumption over a multimillion-year time scale (53). Enhanced weathering during the eruption of the Southern Kerguelen Plateau, as evidenced by calcium and osmium isotopes (30, 54), and increased trace metal abundances in

sediments (27) may have played an important role in decreasing atmospheric CO₂ levels. The relatively mild environmental perturbations caused by the Southern Kerguelen Plateau may have contributed to the occurrence of anoxic conditions in the ocean and affected some species [e.g., heavily calcified nannoconids (55)], but the majority of species survived, possibly due to their ability to adapt to gradual environmental deterioration (13, 55). However, for LIPs that are characterized by rapidly erupting and intense degassing (e.g., Emeishan LIP, Siberian Traps, and CAMP), this mechanism of CO₂ drawdown would be trivial and less effective, as gradual weathering processes could not accelerate fast enough to keep track of volcanic CO₂ emissions. Biota could not tolerate the abrupt and severe environmental changes caused by rapid and intense CO₂ degassing, which ultimately led to their demise.

Our results stress the importance of reducing and slowing down anthropogenic CO₂ emissions in preventing disastrous environmental consequences. The current global anthropogenic CO₂ emission rate is up to 50 Gt·y⁻¹ (56), which is hundreds of times faster than the average rate of outgassing from the Siberian Traps that caused the largest mass extinction in geological history. A caveat here is that CO₂ emission rates of individual pulses of LIPs still need to be better constrained, given that LIP emplacements probably experienced hiatuses (e.g., ref. 11). Such extremely rapid and intense anthropogenic CO₂ emissions may lead to catastrophic and irreversible environmental crises on Earth in the future (e.g., ref. 57). Our study of past volcanism and environmental perturbations indicates that, in order to avoid severe environmental consequences, it is critical to reduce and slow down CO₂ emissions to allow our planet to establish an equilibrium between CO₂ emissions and sinks.

Materials and Methods

Samples. The basaltic samples from Ocean Drilling Program Sites 749, 750, and 1136 were requested from the Kochi Core Center, Japan. A total of 18 thin sections were made from these samples, and, based on thin-section examinations, nine samples that had apparently unaltered plagioclase phenocrysts were selected for ⁴⁰Ar/³⁹Ar dating (*SI Appendix, Tables S1 and S2*). The three samples selected for ⁴⁰Ar/³⁹Ar dating from Site 749 are plagioclase-phyric basalt, with ~40 vol.% of plagioclase phenocrysts (*SI Appendix, Fig. S1*). Samples for ⁴⁰Ar/³⁹Ar dating from Site 750 are from the upper (15R-5) and lower (16R-8) stratigraphic levels of the drilling hole. The former is a pyroxene- and plagioclase-phyric basalt, and the latter is a plagioclase-phyric basalt with ~10 vol.% of plagioclase phenocrysts (*SI Appendix, Fig. S1*). Samples from Site 1136 are plagioclase-phyric basalt with ~10 to 30 vol.% of plagioclase phenocrysts (*SI Appendix, Fig. S1*).

Melt inclusions are present in some plagioclase samples in basalts from Sites 749 and 1136 (Fig. 3 and *SI Appendix, Table S1*). Samples from Site 750 contain very few (mostly ~5% vol.%) plagioclase phenocrysts (*SI Appendix, Fig. S1 and Table S1*), and melt inclusion was not observed. Some melt inclusions from Site 1136 contain a vapor bubble. The melt inclusions are usually ~10 to 20 μm long (Fig. 3). One plagioclase crystal from Site 749 contains gas inclusions that are spherical and less than 10 μm in size (Fig. 3B). Olivine- or pyroxene-hosted melt inclusions were not observed for samples from the Southern Kerguelen Plateau.

The ⁴⁰Ar/³⁹Ar Geochronology. The ⁴⁰Ar/³⁹Ar geochronology analyses of plagioclase separates from basalts from the Southern Kerguelen Plateau were conducted at the Western Australian Argon Isotope Facility in Curtin University. The analytical procedures were the same as those of ref. 42 and are detailed in *SI Appendix*. All parameters and relative abundance values are provided in *Dataset S1* and corrected for blank, mass discrimination, and radioactive decay.

Our criteria for the determination of a robust plateau age are as follows: 1) ⁴⁰Ar/³⁹Ar plateaus obtained from fresh mineral separates are preferred to those from groundmass; 2) ⁴⁰Ar/³⁹Ar plateaus must include at least 70% of the

released ^{39}Ar (15, 58); 3) the plateaus should be defined by at least three consecutive steps consistent at 95% confidence level and satisfying a probability of fit (p) of at least 0.05; and 4) $^{40}\text{Ar}/^{36}\text{Ar}$ intercepts should, ideally, overlap with the atmospheric $^{40}\text{Ar}/^{36}\text{Ar}$ ratio of 298.56 ± 0.31 (59). If the $^{40}\text{Ar}/^{36}\text{Ar}$ composition of the trapped argon measured for a statistically reliable $^{39}\text{Ar}/^{40}\text{Ar}$ – $^{36}\text{Ar}/^{40}\text{Ar}$ isochron ($p > 0.05$) differs from an atmospheric value, then the measured ratio and its uncertainties are used in the age-spectrum model age calculation, following the approach of ref. 60. Miniplateaus are defined similarly, except that they include between 50% and 70% of ^{39}Ar . Miniplateau ages are considered less robust than their plateau counterparts, and are only accepted where there is a corroborating plateau age from a nearby sample.

The $^{40}\text{Ar}/^{39}\text{Ar}$ plateau and isochron ages are summarized in *SI Appendix, Table S2*. The $^{40}\text{Ar}/^{39}\text{Ar}$ age spectra are shown in *SI Appendix, Fig. S2*, and detailed analytical data are provided in *Dataset S1*.

Calculation of the Age of OAE 1a. There have been no direct isotopic age constraints on OAE 1a (e.g., ref. 27). The beginning of OAE 1a is 298 thousand \pm 15 thousand years younger than the end of magnetochron M0, based on orbital tuning (26). The beginning of magnetochron M0 was recently dated at 121.2 ± 0.4 Ma (25), and it lasted for 490 thousand \pm 25 thousand years (26). Therefore, the beginning of OAE 1a is calculated to 120.4 ± 0.4 Ma.

Raman Spectroscopy and CO_2 Density in the Bubbles of Melt Inclusions. Eight doubly polished thick (100- μm) sections were made from basalt samples, in which melt inclusions were recognized in corresponding thin sections (*SI Appendix, Table S1*). We used Raman microspectroscopy to detect and analyze the compositions of the vapor bubbles in unexposed melt inclusions (Fig. 3A) and gas inclusions (Fig. 3B) hosted in plagioclase. The Raman spectra were acquired with a Horiba LabRAM HR Evolution instrument at the Commonwealth Scientific and Industrial Research Organization (CSIRO) laboratories in Perth (Australia), which uses a 532-nm single-frequency 100-mW diode laser and provides 12 mW at the focus point through a 100 \times objective. The grating used was 1,800 grooves per mm.

We detected CO_2 in the vapor bubbles in melt inclusions in thick sections from three core sections in different parts of the stratigraphic column at Site 1136 (*SI Appendix, Table S1*), while CO , CH_4 , H_2 , H_2S , H_2O , and N_2 were not detected (*SI Appendix, Fig. S6*). The Raman spectrum of CO_2 is characterized by two strong bands at $1,285\text{ cm}^{-1}$ and $1,388\text{ cm}^{-1}$, which are called Fermi diad, and two symmetrical weak bands below $1,285\text{ cm}^{-1}$ and above $1,388\text{ cm}^{-1}$, which are called hot bands (Fig. 3E and ref. 61). In this study, we used the OriginLAB software (version 2019b) to determine the positions of the Fermi bands, based on Gaussian-peak fitting of Raman spectra.

The splitting between the Fermi diad (Δ) is proportional to CO_2 density (ρ). At low CO_2 density, there is a linear relationship between Δ and CO_2 density, and their correlation is determined by the type of Raman instrument, gratings, laser-excitation wavelength, and analytical protocols (62). Using the approach of ref. 62, we determined the CO_2 densimeter of this study by measuring the Fermi diad of two known CO_2 density values in our laboratory. The two calibration points are at 5.1 bar at 21.1°C and 32.8 bar at 21.0°C , and two density values of $0.074\text{ g}\cdot\text{cm}^{-3}$ and $0.009\text{ g}\cdot\text{cm}^{-3}$ are calculated by using the equation of state (63), as described by ref. 62, which resulted in two measured Fermi diad (Δ) values of 102.62 cm^{-1} and 102.80 cm^{-1} , respectively (*SI Appendix, Fig. S7*). The fitted equation through these two calibration points is $\rho = -36.093 + 0.3518 \Delta$.

The precision in Δ ($\pm 0.1\text{ cm}^{-1}$) is determined by the error in the peak fitting procedure and corresponds to a precision in fluid density of $0.02\text{ g}\cdot\text{cm}^{-3}$ for inclusions of $1\text{ }\mu\text{m}$ and can be better for larger inclusions (64, 65). The Fermi band position, Δ , and calculated CO_2 densities are provided in *SI Appendix, Table S4*, and detailed Raman spectrum data are available in *Dataset S2*. The results show that the CO_2 densities in the bubbles in melt inclusions range from 0.01 to $0.09\text{ g}\cdot\text{cm}^{-3}$, with an average density of $\sim 0.03\text{ g}\cdot\text{cm}^{-3}$ (*SI Appendix, Table S4*). The CO_2 abundances do not show systematic variations between samples of different ages from different stratigraphic levels (KG59, KG60, and KG61; *SI Appendix, Table S4 and Fig. S3C*), indicating no temporal control on CO_2 abundance.

In sample KG34 from Site 749, there are some bubble-bearing melt inclusions, but neither CO_2 nor other gases was detected in the bubbles of the melt inclusions. This, however, does not mean that there is no CO_2 in the bubbles, as

whether the CO_2 can be detected by Raman spectroscopy is also influenced by many other factors, such as the size of the bubble, the shape of the melt inclusion, the depth of the bubble beneath the mineral surface, and the optical quality of the sample (66). On the other hand, gas inclusions containing relatively high-density CO_2 (up to $0.35\text{ g}\cdot\text{cm}^{-3}$; *SI Appendix, Table S4*) and minor N_2 and H_2O (*SI Appendix, Fig. S6*) were found in plagioclase in this sample, which may indicate that degassed volatiles were encapsulated during the crystallization of plagioclase.

HRXCT Image and Volume of the Bubbles in Melt Inclusion. To study the three-dimensional (3D) distribution and volume percent of the bubble(s) in a melt inclusion, we used the HRXCT technique to image the melt inclusions (Fig. 3D). Microcores were drilled from the thick sections and imaged by using a Zeiss Versa XRM 520 3D X-ray microscope installed at the Australian Resources Research Centre (CSIRO Mineral Resources, Perth) using a voltage of 120 kV, a power of 10 W, and a voxel size of $2\text{ }\mu\text{m}$. The melt inclusions and bubbles were segmented from the grayscale images, and their volume and number were calculated by using Avizo3D (*Dataset S3*).

Except for one melt inclusion that has high bubble-to-melt inclusion volume (34% bubble; *Dataset S3*), the bubble-volume percents of other melt inclusions lie in a small range between 5% and 20% (*SI Appendix, Fig. S8*). Some studies argue that vapor bubbles that were exsolved from the melt after trapping would have a relatively uniform bubble-to-melt inclusion ratio [e.g., 3% bubble (67)] or ratios that do not exceed a certain value [e.g., ~ 6 to $\sim 8\%$ bubble (66)], while melt inclusions that trap both melt and various proportions of vapor during their formation would have a wide range of or relatively high bubble-to-melt inclusion ratios. Although the bubble-to-melt inclusion volume ratios of our samples are mostly higher than the values in those studies, it does not necessitate that the bubbles in our melt inclusions are cotrapped. We suggest that all but one of the vapor bubbles in our study were produced through volatile exsolution after trapping for the following reasons: 1) The aforementioned studies all evaluated melt inclusions in olivine, which are not directly comparable to melt inclusions in other minerals. For example, for pyroxene, some researchers showed that it may contain volatile exsolution bubbles that have a volume percent of 10 to 20% (18), which is different from that of olivine, as shown in refs. 67 and 66. 2) These studies all assume a spherical shape for bubbles in melt inclusions when estimating the volume of the bubbles, which may have somewhat oversimplified the geometry of the bubbles and led to compromised volume estimations that are not as accurate as those obtained by HRXCT 3D imaging. 3) Given that the gas bubbles found in some plagioclase samples have relatively high CO_2 density (average = $0.3\text{ g}\cdot\text{cm}^{-3}$; *SI Appendix, Table S4*), melt inclusions that contain both cotrapped volatile and exsolution volatile would likely have higher measured CO_2 abundance. This is not the case for our melt inclusions since their bubbles have relatively low CO_2 density (0.01 to $0.09\text{ g}\cdot\text{cm}^{-3}$; *SI Appendix, Table S4*).

Calculation of CO_2 Emission Volume of the Southern Kerguelen Plateau. We used a Monte Carlo simulation approach to calculate the total amount of CO_2 emissions from the Southern Kerguelen Plateau volcanism before OAE 1a (i.e., pre-120 Ma; *SI Appendix, Fig. S5*). All the Monte Carlo modelings in this study were performed by using the Excel add-in program QuantumXL by Sigma-Zone. The following parameters and their distributions were used in the Monte Carlo simulation (*SI Appendix, Table S5*):

- 1) CO_2 density in the bubble of melt inclusions. This is measured by Raman spectroscopy and calculated by using the calibrated CO_2 densimeter. We used QuantumXL to fit the distribution of the data, and the results showed that a two-parameter lognormal distribution can best describe the data ($P = 0.85$).
- 2) Bubble volume percent in melt inclusion. This is measured by using HRXCT. The fitting results using QuantumXL show that the measured bubble volume percent (except the outlier 34%) can be described by a Gaussian distribution ($P = 0.12$).
- 3) Percent of CO_2 in bubble vs. in whole melt inclusion. Previous studies have shown that the bubble of a melt inclusion contains the majority of CO_2 of the whole melt inclusion. For example, it was calculated that an average of 61% (67), $\sim 80\%$ (68), and 92% (64) of CO_2 is in the bubble for the melt inclusions measured in these studies. In the Monte Carlo simulation,

we used a uniform distribution from 61 to 92% for the percent of CO₂ in the bubble of a melt inclusion. In addition to the silicate phase of melt inclusions, carbonate crystals on the bubble wall could also be a source of carbon (e.g., refs. 67 and 69). However, carbonates were not observed either from the Raman spectra or HRXCT images.

- 4) The density of the silicate phase of the melt inclusions. We used a value of 2.75 g·cm⁻³ from ref. 64.

These parameters were then used to calculate the total amount of CO₂ in a melt inclusion using the equation in *SI Appendix, Table S5*, which represents the abundance of CO₂ in the Southern Kerguelen Plateau magma.

To calculate the total amount of CO₂ emitted from the Southern Kerguelen Plateau, the following parameters were used in the Monte Carlo simulation (*SI Appendix, Table S5*):

- 5) Basalt density. We used a value of 2.9 g·cm⁻³ from ref. 70.
- 6) Total basalt volume of the Southern Kerguelen Plateau. The areal extent of the Southern Kerguelen Plateau is estimated to be 4.5 × 10⁵ km², and the vertical dimensions were constrained by wide-angle seismic data and gravity modeling (39). Based on the areal and vertical dimensions of the Southern Kerguelen Plateau, the total basalt volume is calculated to be of 8.5 × 10⁶ km³ (39).
- 7) Percentage of pre-OAE basalt volume. Geochronology data show that most of the Southern Kerguelen Plateau basalts erupted before ~120 Ma (this study and refs. 40 and 42), while the southernmost portion erupted at ~113 Ma (Site 738; *SI Appendix, Fig. S5* and ref. 42), postdating OAE 1a. The ages of Site 748 (~97 Ma) are much younger; however, these ages are from sanidine from trachybasalt or basaltic trachy-andesite, which are lithologically different from other sites on the Southern Kerguelen Plateau (42). These evolved volcanic products probably represent a minor late-stage volcanic veneer on the plateau. The boundary between the pre-120-Ma portion and post-120-Ma portion of the Southern Kerguelen Plateau remains unclear. We estimated that 70 to 90% of the Southern Kerguelen Plateau (the area with a solid boundary line in *SI Appendix, Fig. S5*) erupted before OAE 1a (*SI Appendix, Table S5*) and used a uniform distribution for this parameter.
- 8) CO₂ degassing efficiency. It is generally assumed that 100% of CO₂ is degassed by LIP basalts due to the low CO₂ solubility in basaltic melt at atmospheric pressures (e.g., ref. 43). However, 100% degassing efficiency may not be realistic, as erupted basaltic rocks still contain a small amount of volatiles, according to degassing experiments (71), and 80% efficient CO₂ degassing has been adopted by ref. 12. To take a wide range of scenarios into account, we used a CO₂ degassing efficiency ranging from 80 to 100% for the Southern Kerguelen Plateau volcanism in our Monte Carlo simulations (*SI Appendix, Table S5*).

In the Monte Carlo simulation, we conducted 10,000 iterations, and, in each iteration, a random value was used for the uncertain variables, based on the defined probability distributions (*SI Appendix, Table S5*). The calculated CO₂ abundance in melt inclusions from the Southern Kerguelen Plateau is 0.15^{+0.17}_{-0.08} wt.%. The Southern Kerguelen Plateau magma contained a total amount of 0.29^{+0.34}_{-0.12} × 10⁵ Gt CO₂ (uncertainties in the CO₂ volumes and rates herein are quoted at 1σ), and 0.26^{+0.31}_{-0.14} × 10⁵ Gt CO₂ (Table 1 and *SI Appendix, Fig. S9*) was emitted into the atmosphere before OAE 1a.

We note that since these CO₂ emission estimations are based on plagioclase-hosted melt inclusions, there is a possibility that the actual CO₂ emissions of the Southern Kerguelen Plateau could be higher than our estimated values due to the likely CO₂ loss in melt inclusions prior to entrapment and postentrapment crystallization of the plagioclase. It currently remains challenging to restore the original CO₂ concentrations in the melts due to a lack of understanding of how CO₂ may be exchanged between the external melt and inclusions through plagioclase hosts (e.g., ref. 72). Nevertheless, these caveats do not necessarily mean that our estimations are significantly lower than the actual CO₂ emissions and, thus, are inferior to results obtained from the more commonly used olivine- or pyroxene-hosted melt inclusions (e.g., refs. 18 and 47), as it was found in some cases that plagioclase-hosted melt inclusions have similar or even higher CO₂ concentrations than olivine-hosted melt inclusions from the same suite of samples (e.g., ref. 73). In addition, the bubbles in our plagioclase-hosted melt inclusions have similar CO₂ density (Fermi diad spacing) compared with bubbles

in other olivine- and pyroxene-hosted melt inclusions (e.g., refs. 18 and 64), which does not support obvious CO₂ loss for our samples.

Calculation of Carbon-Isotope Excursion. The carbon-isotope change caused by the volcanic degassing of the Southern Kerguelen Plateau can be estimated from a simple mass balance equation (e.g., ref. 19). Based on our melt-inclusion studies, the Southern Kerguelen Plateau magmatism emitted a total amount of 0.26^{+0.31}_{-0.14} × 10⁵ Gt CO₂ into the atmosphere prior to OAE 1a. There have been no available measured carbon-isotope data for the Kerguelen CO₂ emissions. Considering that the Kerguelen LIP and Iceland may have shared a similar plume-ridge interaction-formation mechanism (cf refs. 42 and 74), and both were free of interaction with crustal organic material, we used the carbon-isotope data of the Icelandic CO₂ emissions (75) in our calculation. The early Cretaceous CO₂ reservoir was estimated to be 1.52 × 10⁵ Gt (76), and the δ¹³C value prior to the negative excursion of OAE 1a was ~2.5‰ (22).

Using the lightest δ¹³C value of -5.29‰ that was measured for the Icelandic CO₂ degassing (75), we calculated a δ¹³C value of 1.36‰ after the emplacement of the Southern Kerguelen Plateau, which means that the CO₂ degassing of the Southern Kerguelen Plateau magmatism was not able to cause the negative carbon-isotope excursion of -3 to -5‰ that was observed for OAE 1a (e.g., refs. 27 and 31). We note that this calculation of the carbon-isotope negative excursion should be viewed as maximum estimates, as the Southern Kerguelen Plateau volcanism had been erupting for a few million years before OAE 1a, while the negative excursion at the base of OAE 1a occurred in a short interval of tens of thousands of years (31).

Although we discussed the possibility that the actual CO₂ emissions of the Kerguelen LIP could be greater than our estimations due to possible CO₂ loss in our plagioclase-hosted melt inclusions, to achieve a negative carbon-isotope excursion of -5‰, the CO₂ emissions that were required are at least an order of magnitude greater than our estimated values. This does not seem realistic, considering that our bubbles in plagioclase-hosted melt inclusions have similar CO₂ density with those of olivine- and pyroxene-hosted melt inclusions (e.g., refs. 18 and 64), which indicates no obvious CO₂ loss.

Calculation of CO₂ Emission Volumes of Major LIPs. To assess how the volume of CO₂ emissions from the Southern Kerguelen Plateau volcanism are compared with that of other LIPs, we used a similar Monte Carlo simulation approach to calculate the CO₂ emission volumes of these LIPs. Given that CO₂ emission estimation based on melt-inclusion studies for some LIPs is currently lacking (e.g., Emeishan LIP), we calculated the CO₂ emission of these LIPs based on currently available results obtained from other methods (see below). We note that these estimations and comparisons can be improved by using the same approach of CO₂ emission quantification where possible in the future. It should also be noted that our exercise here is to provide state-of-the-art quantifications of CO₂ emission of these LIPs. Thus, we used the parameters and their uncertainties (if available) reported in the literature, rather than endeavor to improve the quantifications by exploring the uncertainty of the used parameters ourselves.

Siberian Traps. Measurements on olivine-hosted melt inclusions from meimechite of the Siberian Traps yielded low CO₂ concentrations (<1.5 wt%), which were not believed to be representative of the Siberian Traps magma due to decarbonation on ascent of primitive meimechite melts (77). The CO₂ concentrations (<0.07 wt%) in melt inclusions analyzed by ref. 78 are even much lower than that of ref. 77. Therefore, these data are not used in the estimation of the CO₂ emission of the Siberian Traps. In an alternative approach to estimate the CO₂ emission, Sobolev et al. (19) proposed that CO₂ degassed from the Siberian Traps was contained in the recycled oceanic crust and peridotitic components of the plume head. The parameters and their distributions used in the Monte Carlo simulation to calculate the CO₂ emission of the Siberian Traps are as follows (*SI Appendix, Table S6*):

- 1) Percentage of recycled components in the plume head. It was estimated that the source of the Siberian Traps consisted of ~10 to 20 wt.% of recycled oceanic crust components and ~90 to 80 wt.% of peridotitic component (19).
- 2) CO₂ abundance in recycled and peridotitic components. The minimum and maximum estimated CO₂ abundances in recycled oceanic crust are 900 parts per million (ppm) and 1,800 ppm, respectively (19). For the peridotitic component of the Siberian Traps, 70 ppm was used by ref. 19. In our modeling,

we used a uniform distribution from 900 ppm to 1,800 ppm for the recycled component and a constant value of 70 ppm.

- 3) The plume-head volume. The volume of the Siberian mantle plume head was estimated to be 180 million km³ (79).
- 4) CO₂ extraction rate. The thermomechanical model of Sobolev et al. (2011) (19) showed that almost all carbonatite melts from the plume traversed the lithosphere and crust, and a significant part of the volatiles released from the plume finally reached the surface. For these considerations, we use a CO₂ extraction rate of 70 to 100% in the Monte Carlo simulations.

For the above parameters, where the uncertainties were not reported, we treated them as constant in the Monte Carlo simulation, but note that the simulation can be improved when their uncertainties become available.

Using these parameters and a Monte Carlo simulation method (*SI Appendix, Table S6*), we computed that a total amount of $1.30^{+0.35}_{-0.28} \times 10^5$ Gt CO₂ was released (Table 1 and *SI Appendix, Fig. S9*).

Another source of CO₂ emission caused by the Siberian Traps came from metamorphism of organic matter and petroleum due to heating of the Tunguska Basin by the ascending magma. This was mainly generated in two ways (44). First, magma-sedimentary-rock interaction formed breccia pipes, which were rooted in the Cambrian evaporites and were estimated to have a CO₂ production potential of 0.23 to 0.58 Gt per pipe (44). Second, contact aureoles (density = 2.3 g·cm⁻³) of the sill intrusions converted between 0.5 and 1.5 wt.% of organic matter to gas (44). The total number of pipes was estimated to be 6,400 in the Tunguska Basin, and the volume of aureoles was estimated to be 8×10^5 km³ (44). When using the Monte Carlo simulation method to calculate the amount of CO₂ released by the sedimentary rocks, we used a uniform distribution for parameters for which the uncertainty was given and a constant value where the uncertainty was not available (*SI Appendix, Table S6*). This resulted in a total amount of $0.77^{+0.23}_{-0.22} \times 10^5$ Gt sedimentary rock-released CO₂ (Table 1 and *SI Appendix, Fig. S9*).

Combining the magmatic and sedimentary rock-derived CO₂ emissions, the total CO₂ emission caused by the Siberian Traps was $2.08^{+0.40}_{-0.34} \times 10^5$ Gt (Table 1 and *SI Appendix, Fig. S9*).

Emeishan LIP. The amount of magmatic CO₂ degassed from the Emeishan LIP has been estimated by ref. 20 using the same approach as that of ref. 19. In their estimation, the Emeishan mantle plume head was calculated to have a volume of 1×10^8 km³ and is composed of 10 to 20 wt.% recycled oceanic crust component with 900 to 1,500 ppm CO₂, and 80 to 90 wt.% peridotitic component (20). The abundance and amount of CO₂ in the peridotitic component have not been estimated by ref. 20. We used a CO₂ abundance of 70 ppm, according to the estimation of ref. 19. Similar to that of the Siberian Traps, we used a uniform distribution for parameters where the uncertainty was available and a constant value for parameters that lacked uncertainty in the Monte Carlo simulation (*SI Appendix, Table S7*), and we calculated that $0.55^{+0.10}_{-0.09} \times 10^5$ Gt CO₂ was released into the atmosphere (Table 1 and *SI Appendix, Fig. S9*).

The amount of contact metamorphism of sedimentary rock-derived CO₂ was estimated to be ~11 to 26 times larger than that of sill intrusions, which emitted ~5,600 Gt of CO₂ (46). Based on these parameters and their distributions in *SI Appendix, Table S7*, we used a Monte Carlo simulation to compute that the amount of sedimentary rock-derived CO₂ is $(0.75 \text{ to } 1.33) \times 10^5$ Gt (16 to 84 percentiles). Together, the emplacement of the Emeishan LIP could have released $(1.30 \text{ to } 1.88) \times 10^5$ Gt (16 to 84 percentiles) CO₂ (Table 1 and *SI Appendix, Fig. S9*).

CAMP. The CO₂ emission of CAMP was estimated to be up to 10⁵ Gt by ref. 18 using Raman spectrum data of CO₂ in bubbles and nanoscale secondary ion mass spectrometry (NanoSIMS) measurements of CO₂ in glass in pyroxene-hosted melt inclusions from the CAMP basaltic rocks, but uncertainty was not calculated. We use the Monte Carlo simulation method to recalculate the CO₂ emission of CAMP based on the measured parameters of ref. 18:

- 1) CO₂ density in the bubbles of melt inclusions. The Raman spectrum of the bubbles in pyroxene-hosted melt inclusions was measured by ref. 18. When calculating the CO₂ density of the bubbles, the CO₂ densimeter of ref. 65 was used by ref. 18, while the CO₂ densimeter specific to their own instrument was not calibrated. Here, we calculated two CO₂ density values, one using the CO₂ densimeter of ref. 65 and one using our calibrated densimeter, in order for a direct comparison with that of the Kerguelen LIP, and a

Gaussian distribution was used to describe the data as fitted using QuantumXL (*SI Appendix, Table S8*).

- 2) Bubble volume percent in melt inclusion. This was estimated by ref. 18 and ranged from 10 to 20%. We used a uniform distribution for this parameter (*SI Appendix, Table S8*).
- 3) CO₂ abundance in glass of the melt inclusions. This was measured by using NanoSIMS by ref. 18, and we used a Gaussian distribution to describe the data (*SI Appendix, Table S8*).
- 4) The density of the silicate phase of the melt inclusions. The density value of 2.75 g·cm⁻³ from ref. 64 was used.
- 5) Basalt density. We used a value of 2.9 g·cm⁻³ from ref. 70.
- 6) Total basalt volume. This was estimated to be 5×10^6 km³ to 6×10^6 km³ by ref. 18, and we used a uniform distribution in the Monte Carlo simulation.

Using a Monte Carlo simulation approach (*SI Appendix, Table S8*) and the parameters described above (*SI Appendix, Table S8*), we calculated that the volcanic CO₂ emission volume of the CAMP was $0.87^{+0.34}_{-0.26} \times 10^5$ Gt using the CO₂ densimeter of ref. 65 or $0.29^{+0.22}_{-0.22} \times 10^5$ Gt using the CO₂ densimeter of this study.

The thermogenic CO₂ from sill-emplacement-induced contact metamorphism was calculated based on the modeled cumulative CO₂ productions of three boreholes from the Amazonas and Solimões basins in Brazil, including boreholes ATZ (97 t·m⁻²), OAST (52 t·m⁻²), and MAST (103 t·m⁻²), and the basin area of 9×10^5 km² (45). We computed a total amount of $0.75^{+0.26}_{-0.25} \times 10^5$ Gt thermogenic CO₂. The total amount of CO₂ emissions caused by the emplacement of CAMP was computed to be $1.64^{+0.42}_{-0.38} \times 10^5$ Gt or $1.05^{+0.33}_{-0.31} \times 10^5$ Gt (Table 1 and *SI Appendix, Fig. S9*), using the CO₂ densimeter of ref. 18 and this study, respectively.

Karoo and Ferrar LIPs. The amount of CO₂ formed by contact metamorphism of sill intrusions in the Karoo Basin was estimated to be 0.274×10^5 Gt (80); however, there have been no estimates of the magmatic CO₂ emission from the Karoo and Ferrar LIPs.

Central Kerguelen Plateau, Broken Ridge, Caribbean LIP, Ontong Java LIP, High Arctic LIP, and Madagascar LIP. All of these LIPs could have contributed to OAE 2 at ~94 Ma (21, 81, 82). However, the CO₂ emissions of these LIPs, and which one(s) contributed to OAE 2, are yet to be determined.

Deccan Traps. The abundance of CO₂ in melt inclusions from the Deccan Traps was estimated to be 0.23 to 1.2 wt.% by using Raman spectroscopic and NanoSIMS analyses (47). Although ref. 83 calculated a relatively lower CO₂ abundance (<0.2 wt.%) in melt inclusions from the Deccan Traps, their estimation was based on Fourier-transform infrared spectroscopic analyses of the melt phase of unheated or heated (partially homogenized) melt inclusions, and these inclusions still have shrinkage bubbles that may also contain CO₂. The total magma volume of the Deccan Traps is estimated to be 1.3×10^6 km³ (84). Using a similar Monte Carlo simulation method (*SI Appendix, Table S9*), we computed a total amount of $(0.15 \text{ to } 0.40) \times 10^5$ Gt (16 to 84 percentiles) magmatic CO₂, of which $(0.13 \text{ to } 0.35) \times 10^5$ Gt (16 to 84 percentiles) CO₂ (Table 1 and *SI Appendix, Fig. S9*) was released into the atmosphere. The main volumes of Deccan lavas were not emplaced in a sedimentary basin, so there was unlikely to be major CO₂ emission caused by contact metamorphism of sedimentary rocks.

Calculation of Average CO₂ Emission Rates of Major LIPs. Constraining the CO₂ emission rate of LIP magmatism is challenging. This is mainly because volcanic eruptions were not strictly continuous, and quiescent periods that last hundreds to thousands of years existed (e.g., ref. 11), but were not resolvable by geochronological analyses. Here, we calculate an average CO₂ emission rate using the estimated CO₂ emission volumes and the durations of LIP emplacements using a Monte Carlo simulation method to characterize the overall CO₂ degassing intensity during the formation of LIPs.

Southern Kerguelen Plateau. The onset of Southern Kerguelen Plateau volcanism to OAE 1a is constrained by the ⁴⁰Ar/³⁹Ar age of 126.9 ± 2.0 Ma (KG 55 and *SI Appendix, Table S2*). We did not use the seemingly older age of 128.0 ± 4.9 Ma due to the large uncertainty, which prevents providing meaningful information for the onset age of the Southern Kerguelen Plateau volcanism. The age of OAE 1a is calculated to be 120.4 ± 0.4 Ma (see above).

Using a Monte Carlo simulation method (*SI Appendix, Table S5*) and the estimated CO₂ emission volume, we compute an average CO₂ emission rate of $0.005^{+0.003}_{-0.004}$ Gt·y⁻¹ for the Southern Kerguelen Plateau prior to OAE 1a.

Siberian Traps. High-precision U–Pb geochronology data indicate that two-thirds of the total volcanic volume erupted over ~0.3 million years at ~259.9 Ma, before and coeval with the end-Permian mass extinction, with subsequent lavas and sills emplaced in a period of ~0.5 million years (85).

We calculate an average CO₂ emission rate of $0.23^{+0.05}_{-0.04}$ Gt-yr⁻¹ during the emplacement of the Siberian Traps using a similar Monte Carlo simulation approach (SI Appendix, Table S6).

Emeishan LIP. According to the stratigraphic correlation of volcanic sequences of the Emeishan LIP (86), the main phase of basaltic magmatism was best constrained by an ⁴⁰Ar/³⁹Ar age of 260.7 ± 1.2 Ma (recalculated from the age of 260.1 ± 1.2 Ma in ref. 87 using the ⁴⁰K decay constants of ref. 41) from the lower stratigraphic level and a U–Pb age of 259.51 ± 0.21 Ma from the upper stratigraphic level, for a duration of ~1 million years. The main phase of the Emeishan magmatism is synchronous with the end-Guadalupian mass extinction at ~260 to 259 Ma (88).

An average CO₂ degassing rate of $0.13^{+0.12}_{-0.05}$ Gt-yr⁻¹ is calculated for the Emeishan LIP based on the CO₂ volume estimation and the geochronology data (SI Appendix, Table S7).

CAMP. High-precision U–Pb geochronology data show that the CAMP magmatism was emplaced in ~0.6 million years since 201.566 ± 0.031 Ma, which is only ~20 thousand years earlier than the end-Triassic mass extinction (3).

The average CO₂ emission rate is computed to be $0.25^{+0.07}_{-0.06}$ Gt-yr⁻¹ when using the CO₂ densimeter of ref. 65 to calculate the CO₂ emission volume or $0.16^{+0.05}_{-0.05}$ Gt-yr⁻¹ when the CO₂ densimeter of this study is used.

1. P. B. Wignall, Large igneous provinces and mass extinctions. *Earth Sci. Rev.* **53**, 1–33 (2001).
2. V. E. Courtillot, P. R. Renne, On the ages of flood basalt events. *C. R. Geosci.* **335**, 113–140 (2003).
3. T. J. Blackburn *et al.*, Zircon U–Pb geochronology links the end-Triassic extinction with the Central Atlantic Magmatic Province. *Science* **340**, 941–945 (2013).
4. S. Burgess, S. Bowring, T. Fleming, D. Elliot, High-precision geochronology links the Ferrar large igneous province with early-Jurassic ocean anoxia and biotic crisis. *Earth Planet. Sci. Lett.* **415**, 90–99 (2015).
5. N. D. Greber *et al.*, New high precision U–Pb ages and Hf isotope data from the Karoo large igneous province; implications for pulsed magmatism and early Toarcian environmental perturbations. *Results Geochem.* **1**, 100005 (2020).
6. B. C. Rocha *et al.*, Rapid eruption of silicic magmas from the Paraná magmatic province (Brazil) did not trigger the Valanginian event. *Geology* **48**, 1174–1178 (2020).
7. J. Chen, Y. G. Xu, “Permian large igneous provinces and their paleoenvironmental effects” in *Large Igneous Provinces: A Driver of Global Environmental and Biotic Changes*, R. E. Ernst, A. J. Dickson, A. Bekker, Eds. (Geophysical Monograph Series, AGU and Wiley, Hoboken, NJ, 2021), vol. **255**, pp. 417–434.
8. P. Wignall, The link between large igneous province eruptions and mass extinctions. *Elements* **1**, 293–297 (2005).
9. C. Dessert *et al.*, Erosion of Deccan Traps determined by river geochemistry: Impact on the global climate and the ⁸⁷Sr/⁸⁶Sr ratio of seawater. *Earth Planet. Sci. Lett.* **188**, 459–474 (2001).
10. B. A. Black, M. Manga, Volatiles and the tempo of flood basalt magmatism. *Earth Planet. Sci. Lett.* **458**, 130–140 (2017).
11. A. Schmidt *et al.*, Selective environmental stress from sulphur emitted by continental flood basalt eruptions. *Nat. Geosci.* **9**, 77–82 (2016).
12. S. Self, M. Widdowson, T. Thordarson, A. E. Jay, Volatile fluxes during flood basalt eruptions and potential effects on the global environment: A Deccan perspective. *Earth Planet. Sci. Lett.* **248**, 518–532 (2006).
13. M. E. Clapham, P. R. Renne, Flood basalts and mass extinctions. *Annu. Rev. Earth Planet. Sci.* **47**, 275–303 (2019).
14. D. H. Rothman, Thresholds of catastrophe in the Earth system. *Sci. Adv.* **3**, e1700906 (2017).
15. F. Jourdan *et al.*, Karoo large igneous province: Brevity, origin, and relation to mass extinction questioned by new ⁴⁰Ar/³⁹Ar age data. *Geology* **33**, 745–748 (2005).
16. M. T. Jones, D. A. Jerram, H. H. Svensen, C. Grove, The effects of large igneous provinces on the global carbon and sulphur cycles. *Palaeogeogr. Palaeoclimatol. Palaeoecol.* **441**, 4–21 (2016).
17. L. Johansson, S. Zahirovic, R. D. Müller, The interplay between the eruption and weathering of large igneous provinces and the deep-time carbon cycle. *Geophys. Res. Lett.* **45**, 5380–5389 (2018).
18. M. Capriolo *et al.*, Deep CO₂ in the end-Triassic Central Atlantic Magmatic Province. *Nat. Commun.* **11**, 1670 (2020).
19. S. V. Sobolev *et al.*, Linking mantle plumes, large igneous provinces and environmental catastrophes. *Nature* **477**, 312–316 (2011).
20. J. Zhu *et al.*, Recycled carbon degassed from the Emeishan plume as the potential driver for the major end-Guadalupian carbon cycle perturbations. *Geosci. Front.* **12**, 101140 (2021).
21. E. Erba, Calcareous nannofossils and Mesozoic oceanic anoxic events. *Mar. Micropaleontol.* **52**, 85–106 (2004).
22. A. P. Menegatti *et al.*, High-resolution δ¹³C stratigraphy through the early Aptian “Livello Selli” of the Alpine Tethys. *Paleoceanography* **13**, 530–545 (1998).
23. X. Zhang, S. Li, X. Wang, X. Zhao, T. Yin, Expression of the early Aptian Oceanic Anoxic Event (OAE) 1a in lacustrine depositional systems of East China. *Glob. Planet. Change* **196**, 103370 (2021).
24. P. B. Wignall, R. J. Twitchett, Oceanic anoxia and the end Permian mass extinction. *Science* **272**, 1155–1158 (1996).
25. Y. Zhang *et al.*, Magnetostratigraphy of U–Pb-dated boreholes in Svalbard, Norway, implies that magnetochron M0r (a proposed Barremian–Aptian boundary marker) begins at 121.2 ± 0.4 Ma. *Geology* **49**, 733–737 (2021).

Deccan Traps. High-precision geochronology data show that the main volume of the Deccan Traps erupted in less than 1 million y at ~66 Ma (e.g., refs. 89, and 90).

We calculate an average CO₂ emission rate of 0.01 to 0.04 Gt-yr⁻¹ (16 to 84 percentiles) for the Deccan Traps using the CO₂ emission estimation above and the age data (SI Appendix, Table S9).

Data Availability. All study data are included in the article and/or supporting information.

ACKNOWLEDGMENTS. We acknowledge funding from Australian Antarctic Division Science Project 4446. The Kochi Core Center is thanked for the ease of acquiring samples. Q.J. was supported by the China Scholarship Council–Curtin International Postgraduate Research scholarship and a Curtin Publication Grant. AuScope is thanked for financial support toward the Western Australian Argon Isotope Facility. We thank the constructive comments from four anonymous reviewers.

Author affiliations: ^aWestern Australian Argon Isotope Facility, Curtin University, Bentley, WA 6102, Australia; ^bThe Institute for Geoscience Research, School of Earth and Planetary Sciences, Curtin University, Bentley, WA 6102, Australia; ^cJohn de Laeter Centre, Curtin University, Bentley, WA 6102, Australia; ^dTimescales of Mineral Systems Group, Curtin University, Bentley, WA 6102, Australia; ^eDepartment of Earth Sciences, Natural Resources and Sustainable Development, Uppsala University, 752 36 Uppsala, Sweden; ^fCSIRO Energy Resources, Kensington, WA 6151, Australia; ^gGeoscience Atom Probe, Curtin University, Bentley, WA 6102, Australia; and ^hCSIRO Mineral Resources, Kensington, WA 6151, Australia

26. A. Malinverno, E. Erba, T. D. Herbert, Orbital tuning as an inverse problem: Chronology of the early Aptian oceanic anoxic event 1a (Selli Level) in the Cismon APTICORE. *Paleoceanography* **25**, PA2203 (2010).
27. E. Erba *et al.*, Environmental consequences of Ontong Java Plateau and Kerguelen Plateau volcanism. *Geol. Soc. Am. Spec. Pap.* **511**, 271–303 (2015).
28. M. L. G. Tejada *et al.*, Ontong Java Plateau eruption as a trigger for the early Aptian oceanic anoxic event. *Geology* **37**, 855–858 (2009).
29. G. Charbonnier, K. B. Föllmi, Mercury enrichments in lower Aptian sediments support the link between Ontong Java large igneous province activity and oceanic anoxic episode 1a. *Geology* **45**, 63–66 (2017).
30. C. Bottini, A. S. Cohen, E. Erba, H. C. Jenkyns, A. L. Coe, Osmium-isotope evidence for volcanism, weathering, and ocean mixing during the early Aptian OAE 1a. *Geology* **40**, 583–586 (2012).
31. S. Méhary *et al.*, A volcanic CO₂ pulse triggered the Cretaceous Oceanic Anoxic Event 1a and a biocalcification crisis. *Geology* **37**, 819–822 (2009).
32. M. Tejada, J. Mahoney, C. Neal, R. Duncan, M. Petteerson, Basement geochemistry and geochronology of Central Malaita, Solomon Islands, with implications for the origin and evolution of the Ontong Java Plateau. *J. Petrol.* **43**, 449–484 (2002).
33. H. K. H. Olierook, F. Jourdan, R. E. Merle, Age of the Barremian–Aptian boundary and onset of the Cretaceous Normal Superchron. *Earth Sci. Rev.* **197**, 102906 (2019).
34. F. Jourdan, G. Feraud, H. Bertrand, M. Watkeys, P. R. Renne, Distinct brief major events in the Karoo large igneous province clarified by new ⁴⁰Ar/³⁹Ar ages on the Lesotho basalts. *Lithos* **98**, 195–209 (2007).
35. P. R. Renne *et al.*, State shift in Deccan volcanism at the Cretaceous–Paleogene boundary, possibly induced by impact. *Science* **350**, 76–78 (2015).
36. Q. Jiang *et al.*, ⁴⁰Ar/³⁹Ar dating of basaltic rocks and the pitfalls of plagioclase alteration. *Geochim. Cosmochim. Acta* **314**, 334–357 (2021).
37. S. Polteau *et al.*, The Early Cretaceous Barents Sea Sill Complex: Distribution, ⁴⁰Ar/³⁹Ar geochronology, and implications for carbon gas formation. *Palaeogeogr. Palaeoclimatol. Palaeoecol.* **441**, 83–95 (2016).
38. L. Percival *et al.*, Determining the style and provenance of magmatic activity during the Early Aptian Oceanic Anoxic Event (OAE 1a). *Glob. Planet. Change* **200**, 103461 (2021).
39. M. F. Coffin *et al.*, Kerguelen hotspot magma output since 130 Ma. *J. Petrol.* **43**, 1121–1139 (2002).
40. R. A. Duncan, A time frame for construction of the Kerguelen Plateau and Broken Ridge. *J. Petrol.* **43**, 1109–1119 (2002).
41. P. R. Renne, G. Balco, K. R. Ludwig, R. Mundil, K. Min, Response to the comment by W. H. Schwarz *et al.* on “Joint determination of 40K decay constants and 40Ar*/40K for the Fish Canyon sanidine standard, and improved accuracy for 40Ar/39Ar geochronology” by P. R. Renne *et al.* (2010). *Geochim. Cosmochim. Acta* **75**, 5097–5100 (2011).
42. Q. Jiang, F. Jourdan, H. K. Olierook, R. E. Merle, J. M. Whittaker, Longest continuously erupting large igneous province driven by plume–ridge interaction. *Geology* **49**, 206–210 (2021).
43. B. A. Black, S. A. Gibson, Deep carbon and the life cycle of large igneous provinces. *Elements* **15**, 319–324 (2019).
44. H. Svensen *et al.*, Siberian gas venting and the end-Permian environmental crisis. *Earth Planet. Sci. Lett.* **277**, 490–500 (2009).
45. T. H. Heimdal *et al.*, Large-scale sill emplacement in Brazil as a trigger for the end-Triassic crisis. *Sci. Rep.* **8**, 141 (2018).
46. C. Ganino, N. T. Arndt, Climate changes caused by degassing of sediments during the emplacement of large igneous provinces. *Geology* **37**, 323–326 (2009).
47. A. Hernandez Nava *et al.*, Reconciling early Deccan Traps CO₂ outgassing and pre-KPB global climate. *Proc. Natl. Acad. Sci. U.S.A.* **118**, e2007797118 (2021).
48. T. Bralower, P. Fullagar, C. Paull, G. Dwyer, R. Leckie, Mid-Cretaceous strontium-isotope stratigraphy of deep-sea sections. *Geol. Soc. Am. Bull.* **109**, 1421–1442 (1997).

49. C. E. Jones, H. C. Jenkyns, Seawater strontium isotopes, oceanic anoxic events, and seafloor hydrothermal activity in the Jurassic and Cretaceous. *Am. J. Sci.* **301**, 112–149 (2001).
50. J. J. Mahoney *et al.*, *Initial Reports* (Proceedings of the Ocean Drilling Program, Ocean Drilling Program, College Station, TX, 2001), vol. 192.
51. D. M. Raup, J. J. Sepkoski Jr., Periodicity of extinctions in the geologic past. *Proc. Natl. Acad. Sci. U.S.A.* **81**, 801–805 (1984).
52. P. Schulte *et al.*, The Chicxulub asteroid impact and mass extinction at the Cretaceous-Paleogene boundary. *Science* **327**, 1214–1218 (2010).
53. R. A. Berner, *The Phanerozoic Carbon Cycle: CO₂ and O₂* (Oxford University Press, Oxford, UK, 2004).
54. C. L. Blättler, H. C. Jenkyns, L. M. Reynard, G. M. Henderson, Significant increases in global weathering during Oceanic Anoxic Event 1a and 2 indicated by calcium isotopes. *Earth Planet. Sci. Lett.* **309**, 77–88 (2011).
55. E. Erba, C. Bottini, H. J. Weissert, C. E. Keller, Calcareous nannoplankton response to surface-water acidification around Oceanic Anoxic Event 1a. *Science* **329**, 428–432 (2010).
56. IPCC, “Climate change 2014 synthesis report” in *Contribution of Working Groups I, II and III to the Fifth Assessment Report of the Intergovernmental Panel on Climate Change*, C. W. Team, R. K. Pachauri, L. A. Meyer, Eds. (Intergovernmental Panel on Climate Change, Geneva, 2014).
57. A. D. Barnosky *et al.*, Has the Earth’s sixth mass extinction already arrived? *Nature* **471**, 51–57 (2011).
58. G. Féraud, V. Alric, M. Fornari, H. Bertrand, M. Haller, ⁴⁰Ar/³⁹Ar dating of the Jurassic volcanic province of Patagonia: Migrating magmatism related to Gondwana break-up and subduction. *Earth Planet. Sci. Lett.* **172**, 83–96 (1999).
59. J. Y. Lee *et al.*, A redetermination of the isotopic abundances of atmospheric Ar. *Geochim. Cosmochim. Acta* **70**, 4507–4512 (2006).
60. K. F. Oostingh, F. Jourdan, E. L. Matchan, D. Phillips, ⁴⁰Ar/³⁹Ar geochronology reveals rapid change from plume-assisted to stress-dependent volcanism in the Newer Volcanic Province, SE Australia. *Geochim. Geophys. Geosyst.* **18**, 1065–1089 (2017).
61. M. L. Frezzotti, F. Tecce, A. Casagli, Raman spectroscopy for fluid inclusion analysis. *J. Geochem. Explor.* **112**, 1–20 (2012).
62. H. Lamadrid *et al.*, Reassessment of the Raman CO₂ densimeter. *Chem. Geol.* **450**, 210–222 (2017).
63. R. Span, W. Wagner, A new equation of state for carbon dioxide covering the fluid region from the triple-point temperature to 1100 K at pressures up to 800 MPa. *J. Phys. Chem. Ref. Data* **25**, 1509–1596 (1996).
64. M. E. Hartley, J. Maclennan, M. Edmonds, T. Thordarson, Reconstructing the deep CO₂ degassing behaviour of large basaltic fissure eruptions. *Earth Planet. Sci. Lett.* **393**, 120–131 (2014).
65. Y. Kawakami, J. Yamamoto, H. Kagi, Micro-Raman densimeter for CO₂ inclusions in mantle-derived minerals. *Appl. Spectrosc.* **57**, 1333–1339 (2003).
66. E. M. Aster *et al.*, Reconstructing CO₂ concentrations in basaltic melt inclusions using Raman analysis of vapor bubbles. *J. Volcanol. Geotherm. Res.* **323**, 148–162 (2016).
67. L. R. Moore *et al.*, Bubbles matter: An assessment of the contribution of vapor bubbles to melt inclusion volatile budgets. *Am. Mineral.* **100**, 806–823 (2015).
68. A. Shaw, E. Hauri, T. Fischer, D. Hilton, K. Kelley, Hydrogen isotopes in Mariana arc melt inclusions: Implications for subduction dehydration and the deep-Earth water cycle. *Earth Planet. Sci. Lett.* **275**, 138–145 (2008).
69. F. Schiavi *et al.*, Quantifying magmatic volatiles by Raman microtomography of glass inclusion-hosted bubbles. *Geochim. Perspect. Lett.* **16**, 17–24 (2020).
70. J. G. Moore, Density of basalt core from Hilo drill hole, Hawaii. *J. Volcanol. Geotherm. Res.* **112**, 221–230 (2001).
71. Q. Tang, M. Zhang, C. Li, M. Yu, L. Li, The chemical compositions and abundances of volatiles in the Siberian large igneous province: Constraints on magmatic CO₂ and SO₂ emissions into the atmosphere. *Chem. Geol.* **339**, 84–91 (2013).
72. D. A. Neave, J. Maclennan, T. Thordarson, M. E. Hartley, The evolution and storage of primitive melts in the Eastern Volcanic Zone of Iceland: The 10 ka Grímsvötn tephra series (i.e. the Saksunarvatn ash). *Contrib. Mineral. Petrol.* **170**, 1–23 (2015).
73. E. N. Bennett, F. E. Jenner, M.-A. Millet, K. V. Cashman, C. J. Lissenberg, Deep roots for mid-ocean-ridge volcanoes revealed by plagioclase-hosted melt inclusions. *Nature* **572**, 235–239 (2019).
74. S. García, N. O. Arnaud, J. Angelier, F. Bergerat, C. Homberg, Rift jump process in Northern Iceland since 10 Ma from ⁴⁰Ar/³⁹Ar geochronology. *Earth Planet. Sci. Lett.* **214**, 529–544 (2003).
75. P. Barry, D. Hilton, E. Füre, S. Halldórsson, K. Grönvold, Carbon isotope and abundance systematics of Icelandic geothermal gases, fluids and subglacial basalts with implications for mantle plume-related CO₂ fluxes. *Geochim. Cosmochim. Acta* **134**, 74–99 (2014).
76. D. J. Beerling, M. Lomas, D. R. Gröcke, On the nature of methane gas-hydrate dissociation during the Toarcian and Aptian oceanic anoxic events. *Am. J. Sci.* **302**, 28–49 (2002).
77. A. V. Ivanov *et al.*, Volatile concentrations in olivine-hosted melt inclusions from meltechite and melanephelinite lavas of the Siberian Traps Large Igneous Province: Evidence for flux-related high-Ti, high-Mg magmatism. *Chem. Geol.* **483**, 442–462 (2018).
78. B. A. Black, E. H. Hauri, L. T. Elkins-Tanton, S. M. Brown, Sulfur isotopic evidence for sources of volatiles in Siberian Traps magmas. *Earth Planet. Sci. Lett.* **394**, 58–69 (2014).
79. J. Dannberg, S. V. Sobolev, Low-buoyancy thermochemical plumes resolve controversy of classical mantle plume concept. *Nat. Commun.* **6**, 6960 (2015).
80. H. Svensen *et al.*, Hydrothermal venting of greenhouse gases triggering Early Jurassic global warming. *Earth Planet. Sci. Lett.* **256**, 554–566 (2007).
81. J. Scaife *et al.*, Sedimentary mercury enrichments as a marker for submarine large igneous province volcanism? Evidence from the Mid-Cenomanian event and Oceanic Anoxic Event 2 (Late Cretaceous). *Geochim. Geophys. Geosyst.* **18**, 4253–4275 (2017).
82. S. C. Turgeon, R. A. Creaser, Cretaceous oceanic anoxic event 2 triggered by a massive magmatic episode. *Nature* **454**, 323–326 (2008).
83. B. R. Choudhary, M. Santosh, B. De Vivo, G. Jadhav, E. Babu, Melt inclusion evidence for mantle heterogeneity and magma degassing in the Deccan large Igneous Province, India. *Lithos* **346**, 105135 (2019).
84. A. E. Jay, M. Widdowson, Stratigraphy, structure and volcanology of the SE Deccan continental flood basalt province: Implications for eruptive extent and volumes. *J. Geol. Soc. London* **165**, 177–188 (2008).
85. S. D. Burgess, S. A. Bowring, High-precision geochronology confirms voluminous magmatism before, during, and after Earth’s most severe extinction. *Sci. Adv.* **1**, e1500470 (2015).
86. J. Zhu, Z. Zhang, M. Santosh, S. Tan, Z. Jin, Submarine basaltic eruptions across the Guadalupian-Lopingian transition in the Emeishan large igneous province: Implication for end-Guadalupian extinction of marine biota. *Gondwana Res.* **92**, 228–238 (2021).
87. Y. Li *et al.*, ⁴⁰Ar/³⁹Ar age of the onset of high-Ti phase of the Emeishan volcanism strengthens the link with the end-Guadalupian mass extinction. *Int. Geol. Rev.* **60**, 1906–1917 (2018).
88. Q. Wu *et al.*, High-precision U-Pb zircon age constraints on the Guadalupian in West Texas, USA. *Palaeogeogr. Palaeoclimatol. Palaeoecol.* **548**, 109668 (2020).
89. C. J. Sprain *et al.*, The eruptive tempo of Deccan volcanism in relation to the Cretaceous-Paleogene boundary. *Science* **363**, 866–870 (2019).
90. B. Schoene *et al.*, U-Pb constraints on pulsed eruption of the Deccan Traps across the end-Cretaceous mass extinction. *Science* **363**, 862–866 (2019).
91. A. Young *et al.*, Global kinematics of tectonic plates and subduction zones since the late Paleozoic Era. *Geosci. Front.* **10**, 989–1013 (2019).
92. R. A. Rohde, R. A. Muller, Cycles in fossil diversity. *Nature* **434**, 208–210 (2005).